Composites Part B 179 (2019) 107522

Contents lists available at ScienceDirect

Composites Part B

journal homepage: www.elsevier.com/locate/compositesb

Fabrication and anti-crushing performance of hollow honeytubes

Sha Yin [a,b], Huitian Wang [a,b], Jianxing Hu [a,b], Yaobo Wu [a,b], Yongbin Wang [c], Shiqing Wu [c], Jun Xu [a,b,*]

[a] Department of Automotive Engineering, School of Transportation Science & Engineering, Beihang University, Beijing, 100191, China
[b] Vehicle Energy & Safety Laboratory (VESL), Beihang University, Beijing, 100191, China
[c] Beijing Institute of Space Mechanics & Electricity. Beijing, 100098, China

ARTICLE INFO

Keywords:
Honeycomb
Mechanical properties
Finite element analysis (FEA)
Mechanical testing
Micro-architectured materials

ABSTRACT

Honeytubes were architectured materials formed by the hybrid of honeycomb and lattice microstructures, which exhibited great energy absorption capability. In this work, thin-walled hollow honeytubes (HHTs) were further designed, and fabricated using different 3D printing methodologies and electro-chemical deposition technique. The compression results indicated that HHTs could possess smaller relative density and their specific strength be 2.4 and 1.5 times greater than that of solid-walled honeytubes and honeycombs, respectively. Geometrical effects on compressive performance of HHTs were examined, and tube configurations that determined the interactions with ribs were proved to be vital for the specific performance. Meanwhile, foam filled honeytubes could exhibit additional enhancement after properly designed. The specific energy absorption of HHTs especially steel HHTs was proved to have superiority among cellular materials. Hollow honeytubes (HHTs) in the present study had indicated the guidelines to tailor mechanical properties by microstructure design, which would also provide opportunities for artificial intelligence to speed up the development of novel materials.

1. Introduction

Environmental pollution and energy crisis have become two social problems, which makes lightweight be stringent requirements for the development of automotive industry. The present promising lightweight materials used in engineering include high-strength metal, high-performance fiber reinforced composites and cellular materials [1–3]. Architectured materials, which often contain periodic cellular micro-architectures, have attracted wide attention because of their lightweight and unique mechanical properties unattainable before [4–10]. Accordingly, a large amount of work has been focused on structural design and fabrication technologies to develop architecture materials of different length scales with excellent and extraordinary mechanical properties [3,11–18].

Biological materials, on the other hand, often exhibit excellent mechanical properties that benefit from their delicate microstructures. Those bionic factors can be explored to further design new engineering materials. Honeycombs are one of the most successful biomimetic and micro-architectured materials originated from hexagonal wax cells built by honeybees, which are currently widely used. Different architectural topologies were studied, including hexagonal honeycombs, square honeycombs, triangular honeycombs, kagome honeycomb and chiral honeycombs with designable Poisson's ratio [19–22]. Bio-inspired honeycombs containing ordered patterns that extracted from biological tissues have been widely studied. Those inspired by the beetle elytron exhibiting enhanced mechanical properties and energy absorption capabilities [23–25]. Bio-inspired vertex-modified honeycombs represent a significant improvement over regular honeycomb because the tubes change the deformation pattern of bio-inspired honeycomb [26]. More recently, a new type of tube reinforced honeycombs named as Honeytubes, composed of tubes and ribs like beetle elytron inspired honeycombs, has been developed by the hybrid design of hollow pyramidal lattice and square honeycombs, which exhibit advantages in buckling resistance and mechanical property tunability [27,28].

Thin-walled structures have attracted significant interests due to their low density, energy absorption and crashworthiness applications, and architected 3D thin films are widely studied [13,29–33]. In this work, hollow honeytubes (HHTs) were further designed with three-dimensional interconnected films formed based on the previously developed lattice truss reinforced honeycombs (termed as solid-walled honeytubes). Stereolithography (SLA) and Selective Laser Melting (SLM) 3D printing technology were used to fabricate those HHTs either

* Corresponding author. Department of Automotive Engineering, School of Transportation Science & Engineering, Beihang University, Beijing, 100191, China.
E-mail address: junxu@buaa.edu.cn (J. Xu).

https://doi.org/10.1016/j.compositesb.2019.107522
Received 25 June 2019; Received in revised form 4 October 2019; Accepted 8 October 2019
Available online 11 October 2019
1359-8368/

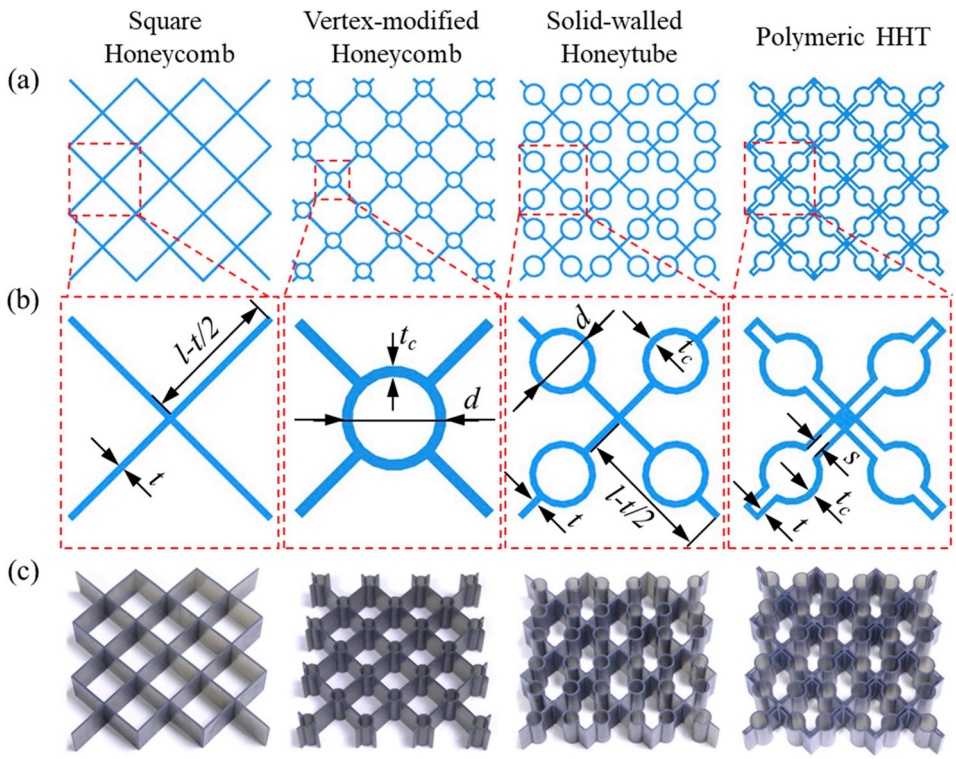

Fig. 1. a) Illustration for polymeric HHTs together with square honeycombs, solid-walled honeytubes and vertex-modified honeycombs; b) representative unit cells for each type of structure and c) the corresponding specimens fabricated by SLA printing.

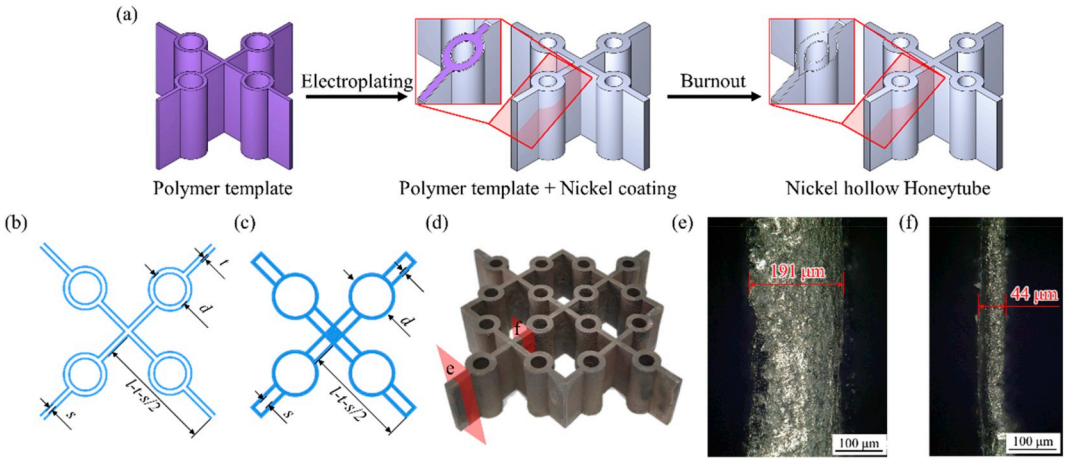

Fig. 2. a) Illustration about the fabrication flowchart for nickel HHT; representative unit cells for b) nickel HHTs and c) steel HHTs with geometrical parameters; d) nickle HHT sample fabricated by electroplating. Cross-section morphology after deposition observed by microscopy around: e) outer ribs; f) intersections.

directly or combined with electro-chemical deposition, which yielding polymeric, steel and nickel HHTs. The anti-crushing performance were studied experimentally, and effects of architectures were studied through simulation. Finally, the energy absorption capability of these hollow honeytubes was examined and compared with other competing counterparts.

2. Experimental

2.1. Polymeric HHTs

Hollow honeytubes (HHTs) were newly designed in this study with three-dimensional interconnected films based on the previous developed solid-walled honeytubes [27,28] as shown in Fig. 1a, together with the corresponding square and vertex-modified honeycombs. The representative unit cell for each type of structure was shown in Fig. 1b together with geometrical illustrations. Polymeric HHTs were fabricated using stereolithography (SLA) based 3D printing technology, which enabled the fabrication of samples with complicated geometries. Using an ultraviolet laser, photosensitive resin was scanned according to the shapes designed and cured layer by layer at room temperature. A toughened resin possessed good fracture elongation of 24% was selected to facilitate large deformation of all the structures during the following tests. All the printed specimens with 3*3 unit cells were shown in Fig. 1c.

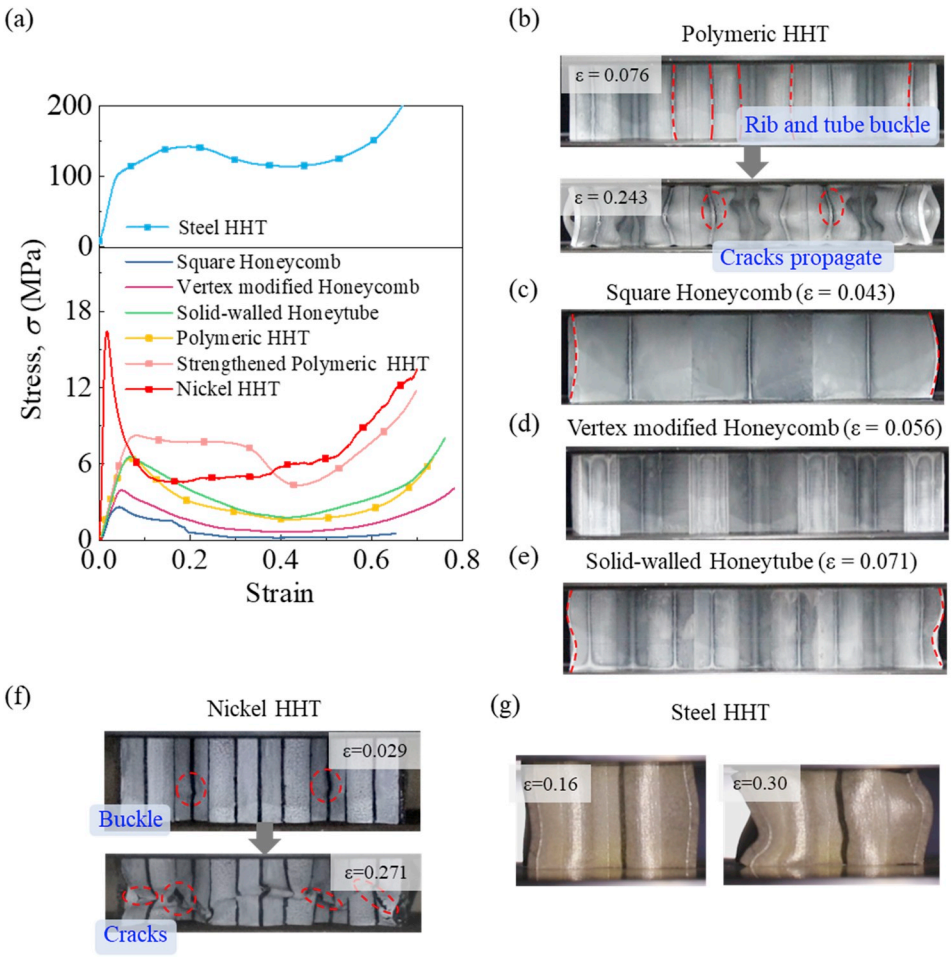

Fig. 3. a) Compressive stress-strain of all types of structures; deformation history of b) polymeric HHT and c) square honeycombs, d) vertex modified honeycombs, e) solid-walled honeytubes, f) nickel HHT and g) steel HHT.

2.2. Metallic HHTs

2.2.1. Nickel HHTs by electro-chemical deposition

Subsequently, Nickel HHTs were also fabricated following three main steps as illustrated in Fig. 2a: (1) Polymeric solid-walled honeytubes were first printed as template using a castable wax resin which was designed for casting molds manufacturing and could be completely burned out. (2) Then, the polymeric templates were immersed in coarse solution (composed of chromic acid and sulfuric acid) to increase surface roughness so that ions can be absorbed on the structure. After that the polymeric templates were subsequently immersed in stannous chloride solution and palladium chloride solution to make the surface prepared for electroless plating. (3) Nickel film was then deposited onto the template's surface through electrochemical deposition in this step. During this process, the polymeric templates after surface modification were first immersed in an electroless plating solution for about 2 h. Then, electroplating was subsequently employed at a current density of 2 A/dm^2 for about 5 h (4) All the samples were then heated in a muffle furnace to burnout the template and the hollow honeytube structures were obtained.

The representative unit cell of obtained metallic HHTs based on solid-walled honeytubes was shown in Fig. 2b, possessing additionally upper and lower surfaces featuring closed ribs. The obtained nickle-plated HHTs specimens were shown in Fig. 2d with cross-section morphologies illustrated in Fig. 2e and f. The nickel film thickness in outer ribs (Fig. 2e) was about 0.2 mm while that near intersections (Fig. 2f) only about 0.04 mm, which was quite uneven and should be attributed to the uneven current distribution in such complex microstructures during electroplating.

2.2.2. Steel HHTs by 3D printing

Besides, another type of metallic HHT was fabricated directly by selective lase melting (SLM) 3D printing technology with 316L stainless steel as raw material. SLM technology used a laser beam with power of about 200 W to object into metallic powder which makes the powder melt and combine together, and the whole structure will finally form layer by layer. The representative unit cell of steel HHTs was shown in Fig. 2c.

The corresponding relative densities for all types of structures, defined as the ratio of solid volume to that of the representative unit cell, were respectively deduced as:

$$\bar{\rho}=\begin{cases} 2t/l, & \text{For Square honeycomb} \\ [2(2l-d)t+\pi dt_c]/2l^2, & \text{For Vertex}-\text{modified honeycomb} \\ [2(l-d)t+2\pi dt_c]/l^2, & \text{For Square honeytube} \\ [4(l-d)t+2\pi dt_c-2st]/l^2, & \text{For Polymeric HHT} \\ [(2l-2d-s)+\pi(2d-2s)-2s]2t/l^2+ & \\ \left[\left[4(l-d)s-s^2+4\pi(d-s)s\right]t\right]/l^2H, & \text{For nickel HHT} \\ [4(l-d)t+2\pi dt_c-2st]/l^2 & \text{For steel HHT} \end{cases} \quad (1)$$

where l was grid length of honeycombs; t was rib thickness; t_c and d were wall thickness and outer diameter of hollow trusses; s was the wall gapping distance in the rib of HHTs as illustrated in Figs. 1–2; H was the height of the structures, which was 20 mm for all the samples. Note that measured relative densities of polymeric structure were 10% lower than

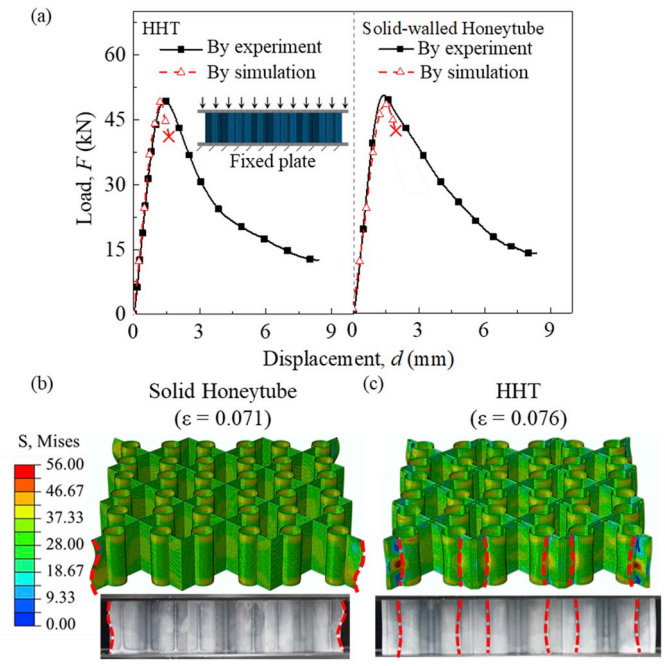

Fig. 4. Comparison between experimental and simulational results for HHTs and solid-walled Honeytubes: a) compressive stress-strain curves; the corresponding failure modes of b) solid-walled Honeytubess and c) HHTs.

that obtained from Eq. (1), while 10% greater for those of steel HHTs and about 40% lower for Ni HHTs, which was attributed to the uneven wall thickness either by 3D printing or electrodeposition.

2.3. Compression experiments

Out-of-plane compression tests were conducted on all the specimens with hydraulic servo testing machine (Instron 8801) at a loading speed of 1.2 mm/min following ASTM C365/C365M. At least three tests were carried out for each type of specimens to ensure repeatability. The compressive stress-strain curves were plotted in Fig. 3 along with deformation history and failure modes. The representative compressive response of polymeric HHTs was typical of cellular solid. The nominal stress increased almost linearly with nominal strain until reaching a stress peak accompanying with rib and tube buckling, followed by crack propagation at the rib-tube or rib-rib intersections. However, the buckling mode for each type of structures was different as shown in Fig. 3c–e. For Ni HHTs, the representative compressive stress-strain curves was similar with those for polymer HHTs. Differently, after reaching the stress peak, the inner cross connections buckled first as indicated in Fig. 3f and then followed by tube buckling. Besides, cracks appeared at the folding edge as further compressed, which wasn't observed in the case of polymeric HHTs, and can be attributed to the nature of electroplated nickel. Besides, for steel HHTs, the stress-strain curve had two linear stages with different slopes before reaching the peak accompanying with rib buckling followed by tube buckling as shown in Fig. 3g. Subsequently, the stress decreased slightly with strain without obvious crushing happened before densification. The mean crushing force (MCF) of steel HHTS was much greater than that of other structures, which indicated good energy absorption capability of steel HHTs by 3D printing.

3. Finite element analysis

3.1. Method

Finite element analysis was carried out to study the mechanical performance of HHTs and assist further optimal design based on Abaqus/Explicit. The structures were sandwiched between two rigid plates, as illustrated in Fig. 4a. All the honeytube structures were modeled using SHELL element S4R while loading plates were modeled using S4R element. Mechanical properties of 3D-printed toughened resin with density $\rho = 1.3\ g/cm^3$, were tested following ASTM D695 (see supplementary materials) with Young's modulus $E = 700$ MPa, yield strength $\sigma = 40$ MPa, and Poisson's ratio $\upsilon = 0.45$. Through mesh convergence analysis, the mesh size were chosen as 0.4 mm for honeytube structures and 2 mm for the loading plates. The lower plate was fixed during compression, while the upper one can only move through compression direction. Automatic self-contact was used for the self-interaction of honeytubes while surface-to-surface contact between structures and loading plates with a validated friction coefficient $\mu = 0.5$ here.

3.2. Validation

The simulational compressive responses of polymer HHTs and solid-walled honeytubes were both plotted in Fig. 4a, which agreed well with experimental results (refer to stiffness and strength values). Also, the buckling mode at the stress peaks was rather similar as shown in Fig. 4b and c. However, discrepancies still existed after the stress peaks as further compressed, which should be attributed to the post-buckling behaviour and complex self-contact conditions that were difficult to predict accurately. Note that the post-buckling behaviour was not to be studied in the present paper, and hence the simulation model would be adopted for further parametric discussion.

Table 1
Summary of geometries and mechanical properties for different types of honeycombs and honeytubes tested.

Structural type	Square honeycomb	Vertex-modified honeycomb	Solid-walled honeytubes	Polymeric HHT	Nickel HHT	Steel HHT
l (mm)	20.5	10.25	20.5	20.5	22.5	20
t (mm)	1	1	1	0.8	0.2	0.6
d (mm)	-	8	8	9.6	8	8
t_c (mm)	-	0.8	0.8	0.8	0.2	0.6
s (mm)	-	-	-	1	1	1
H (mm)	20	20	20	20	20	20
$\overline{\rho}_{equation}$	0.098	0.215	0.155	0.194	0.0581	0.150
$\overline{\rho}_{measured}$	0.085	0.186	0.135	0.186	0.033	0.173
$\rho(kg/m^3)$	111.06	241.98	175.87	242.27	293.75	1381.58
σ(MPa)	2.61	3.92	6.56	6.42	16.45	142.08
E (MPa)	107.76	104.89	129.32	125.63	1624.33	2939.46
$\overline{\sigma}(MPa/(kg/m^3))$	0.0235	0.0162	0.0373	0.0265	0.0560	0.1028
$\overline{E}(MPa/(kg/m^3))$	0.9703	0.4335	0.7353	0.5186	5.5295	2.1276
SEA (J/g)	1.62	6.42	8.69	11.77	9.48	45.23

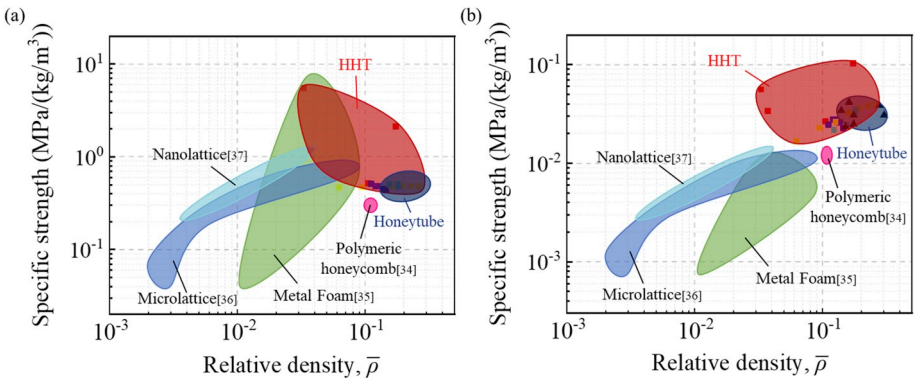

Fig. 5. Ashby chart for a) specific strength and b) specific stiffness against relative density of HHTs comparing with other materials.

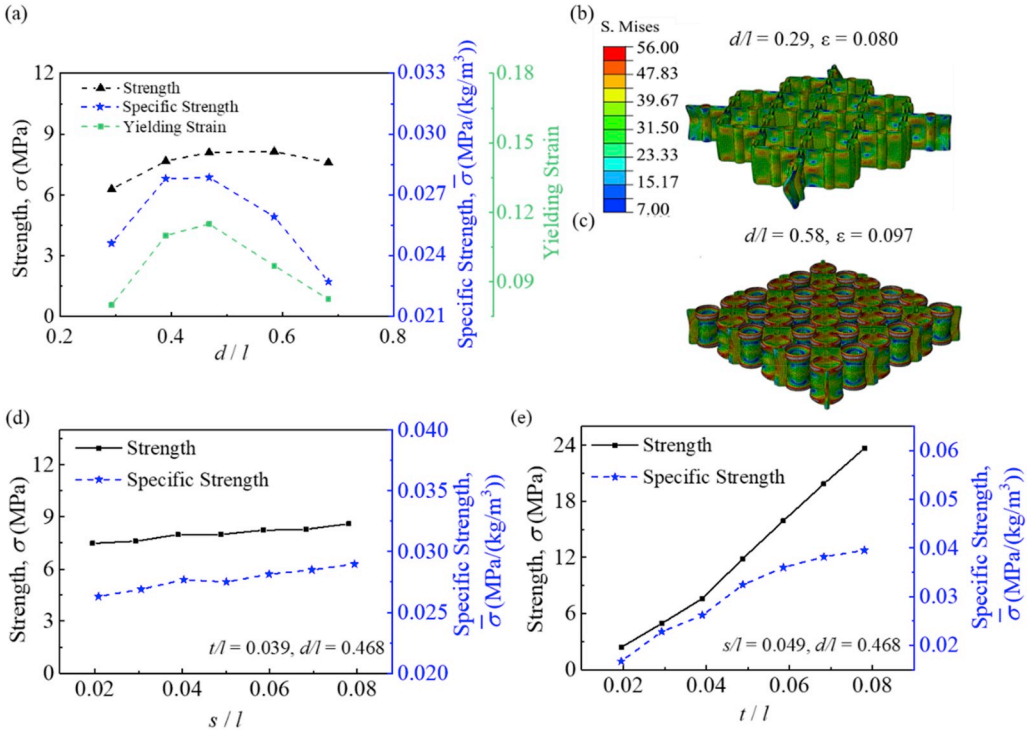

Fig. 6. a) The variation of strength, specific strength and yielding strain with d/l; the corresponding failure modes at the stress peak for HHTs with b) $d/l = 0.29$ and c) $d/l = 0.58$; the variation of strength, specific strength of HHTs with different normalized geometries d) s/l and e) t/l.

4. Discussion

4.1. Compressive properties

The compressive stiffness and strength, E and σ, for all HHTs with different raw materials under compression were calculated and compared with other counterparts as summarized in Table 1. The stiffness and strength values of polymeric HHTs were comparable with those of solid-walled honeytubes; polymer HHTs were respectively approximately 1.16 and 1.20 times stiffer, while 2.46 and 1.64 times stronger than square honeycomb and vertex-modified honeycomb. Meanwhile, nickel HHTs proved to be 12.93 times stiffer and 2.62 times stronger, while steel HHTs were 23.40 stiffer and 22.12 times stronger than polymeric HHTs. In terms of specific stiffness and strength, defined as E/ρ and σ/ρ, where ρ is the measured density of each sample, HHTs outperformed honeycomb constructions and could be superior than the corresponding solid-walled honeytubes. Steel HHTs in this study showed the greatest specific strength, again demonstrating the superiority of HHT architectures. Ashby charts for specific stiffness/strength versus relative density, focusing on the micro-architectures without considering the property contribution of parent materials, were plotted and compared with other cellular materials as shown in Fig. 5. HHTs could possess greater specific mechanical properties than other counterparts, such as polymeric hexagonal honeycombs [34], metal foam [35], microlattice [36] and even nanolattice [37]. When comparing with solid-walled honeytubes, HHTs could also be designed lighter with greater specific mechanical properties. However, HHTs did not always outperform the corresponding solid-walled honeytubes. Then, those HHTs with different normalized geometries (d/l, s/l, t/l) were modeled and analyzed, to explore how structural geometries influence and optimize the mechanical properties.

4.2. Effects of geometries

For effects of d/l, honeytube structures with various d/l were virtually tested with the other two parameters fixed at $s/l = 0.0488$ and $t/l = 0.0390$. The strength, specific strength and yield strain at the peak stress were compared in Fig. 6a, from which all the data increased first

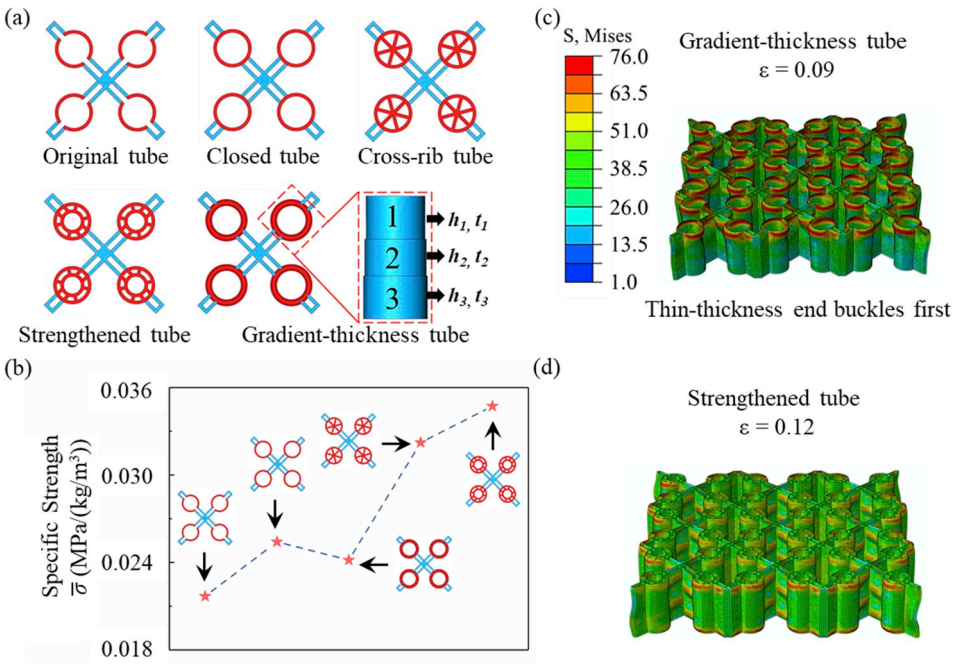

Fig. 7. a) Illustrations of five hollow honeytubes with different tube configurations; b) the specific strength for the corresponding structures comparing with that of original HHTs; failure modes of hollow honeytubes with c) gradient-thickness tubes and d) bamboo-inspired tubes at the corresponding stress peak.

and then decreased with d/l, indicating an optimal d/l existed for the greatest strength and specific strength values. The optimal nominalized tube diameter should be related to the failure mode transition as d/l varied. As shown in Fig. 6b, as d/l is relatively small, the ribs and tubes of HHTs exhibited one-half-wave buckling behavior; meanwhile, as d/l is relatively large, different higher-order buckling behavior was observed and thus tube-rib interaction was stronger.

For effects of normalized rib geometries, structures with different s/l and t/l were modeled and analyzed. The variation of strength and specific strength with s/l and t/l were plotted in Fig. 6d and e, respectively.

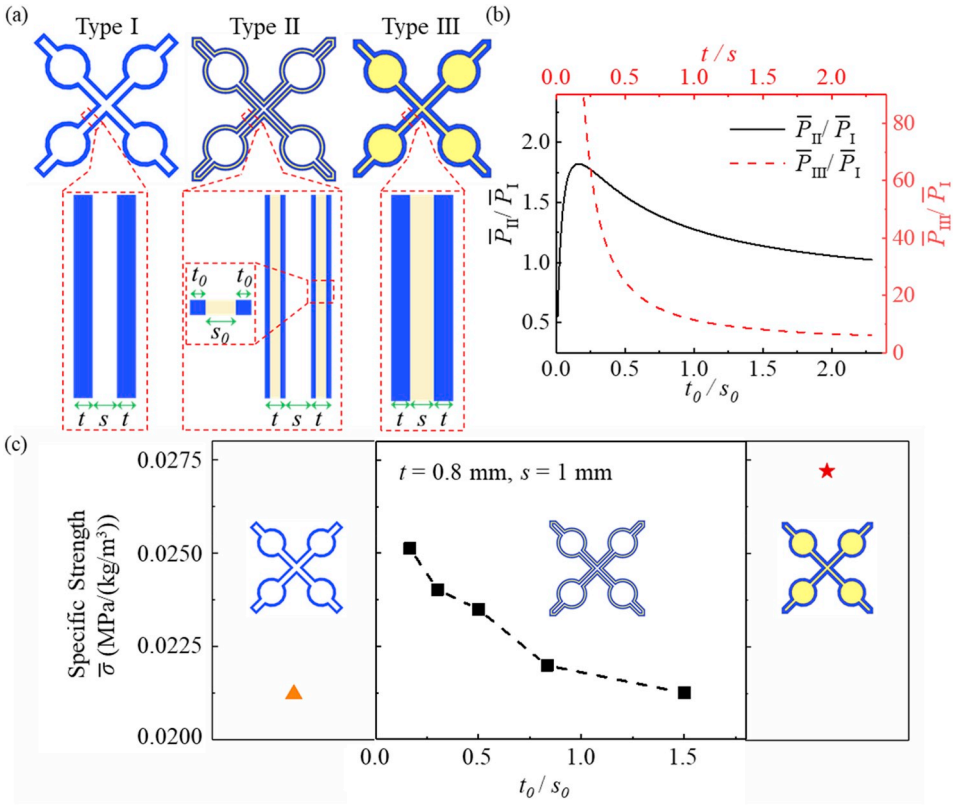

Fig. 8. a) Illustration of two novel types of HHTs after employing sandwich strategy comparing with original HHTs; b) the strengthening effects against thickness ratios in sandwich ribs; c) specific strength comparison among the three types of honeytubes.

The strength and specific strength vary little with s/l as shown in Fig. 6d, which may be attributed to the weak coupling effect between the two thin-walled plates in each rib. The two plates deform individually when being compressed, and thus the rib gapping distance plays an inconsequential role in the mechanical performance of HHT. In contrast, the strength and specific strength increase significantly as t/l increases as shown in Fig. 6e. The failure mode of HHTs are combinations of tube and rib failure because the elastic buckling resistance of plates is strongly improved [38].

4.3. Effects of tube configurations

The tube geometries will affect tube-rib interactions and the mechanical performance of HHTs [27,28]. In this section, four additional tube configurations were designed, including those with closed tube, cross-rib tube, multi-cell strengthened tube and gradient-thickness tube as shown in Fig. 7a, and examined by FE analysis comparing with original HHT. Note that the "original tube" model was the same structures tested in the experimental section, and the "cross-rib tube" model and "strengthened tube" model were both bionic design inspired from bamboo [39]. In the gradient-thickness tube, we take $h_1 = h_3 = 7$ mm, $h_2 = 6$ mm; $t_1 = 0.8$ mm, $t_2 = 1.2$ mm and $t_3 = 1.6$ mm. The specific strength values of HHTs with four novel tube configurations were plotted and compared with original ones as shown in Fig. 7b. The specific strength for structures with closed tubes is about 17.6% greater than that for structures with original tubes, which explicates the importance of tube integrity in structural strengthening, and can also explain the unexpected results that the un-closed HHTs do not outperform the corresponding solid-walled honeytubes in the experimental section. Note that all the models in section 4.1 contain closed tubes for analysis. Furthermore, among the other three tube configurations, HHTs with gradient-thickness tubes exhibit relatively poor mechanical performance, even poorer than those with closed tubes. The corresponding failure mode was shown in Fig. 7c, and the thinner-wall end buckled first at a very small yield strain of $\varepsilon = 0.090$ while $\varepsilon = 0.105$ for those with closed tubes. The uneven stress state in this kind of tubes led to early tube buckling and thus reduced load bearing capacity. In contrast, the specific strength for HHTs with cross-rib tubes and strengthened tubes were 26.8% and 36.6% greater than those with original tubes, respectively. The failure mode of HHTs with strengthened tubes was shown in Fig. 7d. The complex internal tube microstructures could increase the buckling resistance of tubes and thus be vital to increase the corresponding load bearing capacity of HHTs. Based on the above study, polymeric HHTs with strengthened tubes were printed and studied as well. During compression, a stress plateau stage appeared after the stress peak which is the 1.28 times stronger than that of the non-strengthened ones and also showed the potential in energy absorption.

4.4. Effects of sandwich constructions

As we mentioned before, the inducing of thin-walled structures had broadened the designability of Honeytube structures. In our previous study, we had demonstrated hierarchical structures by incorporating sandwich construction possesses greater mechanical performance than their non-hierarchical counterparts [11,40,41]. Accordingly, to further improve the specific properties of HHTs, a similar strategy was adopted and two types of sandwich constructions were designed comparing with the original monolithic one (termed as Type I here) as shown in Fig. 8a accompanying with the critical geometries. Type II was a sandwich-walled honeytube while Type III the original HHT filled the inner space with polyurethane foam. Mechanical properties of these three structures were examined through FE analysis. The mechanical properties of polyurethane foam used in this study were: Young's modulus $E = 110$ MPa, yield strength $\sigma = 3$ MPa, density $\rho = 0.2$ g/cm^3, and Poisson's ratio $\upsilon = 0.4$ [42]. For a honeycomb unit cell of side-length l_0 and height h_0 subjected to an out-of-plane compressive load, the critical load for elastic buckling read $P_{buck} = K\pi^2 D/l_0^2$, where K was the buckling coefficient depending on the constraint conditions at the boundaries, and D the bending stiffness of the constituent honeycomb ribs [38]. When sandwich ribs (Type III honeytubes) were utilized to form the corresponding honeycombs, the overall bending stiffness D could be expressed by neglecting the contribution of foam core as $D = \frac{E_f}{1-\nu_f^2}\frac{t_0(s_0+t_0)^2}{2}$, where E_f and ν_f are the Young's modulus and Poisson's ratio of face sheet, t_0 and s_0 are respectively the thickness of face sheet and foam core. The critical buckling load for honeytubes were thus analyzed by simplifying the tube-integrated ribs as original ribs while neglecting the shape factor after integrating tubes. Accordingly, the corresponding specific buckling load for each type of honeytube was given as followed:

$$\begin{cases} \overline{P_I} = \dfrac{K\pi^2 E_f}{1-\nu_f^2}\dfrac{t^3}{6}\dfrac{1}{2t\rho_f} & \text{For Type I} \\ \overline{P_{II}} = \dfrac{K\pi^2 E_f}{1-\nu_f^2}\dfrac{t_0(t_0+s_0)^2}{2}\dfrac{1}{2t_0\rho_f + s_0\rho_c} & \text{For Type II} \\ \overline{P_{III}} = \dfrac{K\pi^2 E_f}{1-\nu_f^2}\dfrac{t(t+s)^2}{2}\dfrac{1}{2t\rho_f + s\rho_c} & \text{For Type III} \end{cases} \tag{2}$$

The enhancement effect after employing sandwich constructions comparing with Type I honeytubes can be plotted in Fig. 8b and then analyzed. For Type II honeytubes, the enhancement ratio $\overline{P_{II}}/\overline{P_I}$ increased with t_0/s_0 first and then decreases, indicating that an optimal t_0/s_0 existed for the best performance; meanwhile, Type III honeytubes exhibited a much stronger enhancement effect and could always outperform Type I HHTs in terms of specific strength whatever the value t/s was.

These three types of honeytubes were further studied by finite element simulation with various geometries. All the specific strength were calculated and compared in Fig. 8c. The specific strength of Type II honeytube model decreased as t_0/s_0, and equalled to that of Type I honeytube model as $t_0/s_0 = 1.5$. Moreover, the specific strength of Type III honeytube was the greatest, which again indicated the advantages by filling the HHT ribs with lightweight foams. The load could not be transferred through the gap between the two rib plates in either Type I or Type II structures, which had affected the structural stability and load-bearing capacity.

4.5. Energy absorption

Steel HHTs exhibited relatively higher mean crushing force (MCF), which increased their energy absorption capability. According to simplified super folding Element (SSFE) [43–46], mean crushing force for steel HHTs can be theoretically deduced (see supplementary materials). Energy absorption capacities were then analyzed and compared, which defined as the area under the force-displacement curve given as $W = \int_0^{\varepsilon_D} F ds$. ε_D was the densification strain calculated by $(d\psi(\varepsilon)/d\varepsilon)|_{\varepsilon=\varepsilon_D} = 0$, where ψ is the absorption efficiency defined by $\psi = \int_0^{\varepsilon} \sigma(\varepsilon)d\varepsilon/\sigma(\varepsilon)$. Then the specific energy absorption (SEA), defined as energy absorption per unit mass SEA $= W/m$, were summarized in Table 1. Among all HHTs structures in this work, steel HHTs have the best energy absorption capacity, while polymer and nickel HHTs was limited by the fabrication process and properties of parent materials as well. SEA of HHT structures were compared with other structures and also ploted with relative densities as shown in Fig. 9. HHT structures could outperform solid-walled honeytube, polymer foams [47], metallic foams [48], metallic lattices [49] and steel lattice-honeycombs [50], showing promising potential in energy absorption capacity.

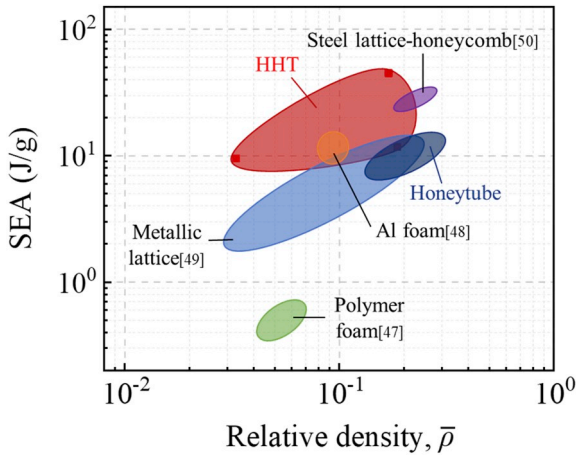

Fig. 9. Ashby chart for SEA against relative density of HHT structures comparing with other cellular materials.

5. Conclusions

Hollow honeytubes (HHTs) were designed with interconnected films and then fabricated through different approaches including 3D printing and electro-chemical deposition, yielding polymer HHTs, nickel HHTs, and steel HHTs. Those HHTs with various geometries, tube configurations and sandwich ribs were comprehensively studied experimentally, analytically and computationally. Hollow honeytubes (HHTs) in the present study have provided further guidelines for designing and optimizing architectured structures.

- HHTs could outperform solid-walled honeytubes and bio-inspired honeycombs, but stress concentration and cracks were readily to initiate at the tube-rib intersections.
- The additionally normalized geometry s/l exhibited slight influences by simulation, due to the weak coupling effects between the two parallel rib walls of HHTs; meanwhile, normalized geometries t/l and d/l exhibited similar effects on compressive performance of HHTs comparing with that of solid-walled counterparts.
- Tube configurations, especially tube completeness and stiffeners were vital for the specific performance of HHTs. Those with strengthened tubes which had stronger interaction with rib walls, exhibited the greatest specific strength among all the configurations discussed and also exhibited excellent energy absorption potential.
- Foam sandwich constructions were incorporated to further increase the specific performance of HHTs. Theoretical analysis and FE simulational results revealed that HHTs after filling with foam, could exhibit much stronger enhancement than sandwich-walled HHTs which outperformed the original Type I HHTs only with selected t_0/s_0.
- Steel HHTs exhibited high mean crushing force and the specific energy absorption of HHTs could surpass most of existing cellular counterparts.

Microstructure design can tailor mechanical properties of lightweight materials, which have provided opportunities to combine artificial intelligence (AI) into materials design and deserve future efforts.

Acknowledgments

This work was financially supported by the National Key Research and Development Program of China (2017YFB0103703), the Fundamental Research Funds for the Central Universities, Beihang University, Young Elite Scientist Sponsorship Program by CAST and the fourth batch of pre-research projects in the manned space field 040202.

Appendix A. Supplementary data

Supplementary data to this article can be found online at https://doi.org/10.1016/j.compositesb.2019.107522.

References

[1] Fleck NA, Deshpande VS, Ashby MF. Micro-architectured materials: past, present and future. P Roy Soc A Math Phy 2010;466:2495–516.
[2] Ashby MF, Bréchet YJM. Designing hybrid materials. Acta Mater 2003;51:5801–21.
[3] Yin S, Chen H, Wu Y, Li Y, Xu J. Introducing composite lattice core sandwich structure as an alternative proposal for engine hood. Compos Struct 2018;201:131–40.
[4] Liu Y, Wang L. Enhanced stiffness, strength and energy absorption for co-continuous composites with liquid filler. Compos Struct 2015;128:274–83.
[5] Liu Y, Schaedler TA, Chen X. Dynamic energy absorption characteristics of hollow microlattice structures. Mech Mater 2014;77:1–13.
[6] Liu Y, Schaedler TA, Jacobsen AJ, Chen X. Quasi-static energy absorption of hollow microlattice structures. Compos B Eng 2014;67:39–49.
[7] Bauer J, Meza LR, Schaedler TA, Schwaiger R, Zheng X, Valdevit L. Nanolattices: an emerging class of mechanical metamaterials. Adv Mater 2017;29.
[8] Li Y, Chen Y, Li T, Cao S, Wang L. Hoberman-sphere-inspired lattice metamaterials with tunable negative thermal expansion. Compos Struct 2018;189:586–97.
[9] Chen Y, Li T, Scarpa F, Wang L. Lattice metamaterials with mechanically tunable Poisson's ratio for vibration control. Phys Rev Appl 2017;7.
[10] Xu B, Yin S, Wang Y, Li H, Zhang B, Ritchie RO. Long-fiber reinforced thermoplastic composite lattice structures: fabrication and compressive properties. Compos Appl Sci Manuf 2017;97:41–50.
[11] Yin S, Wu L, Nutt S. Stretch–bend-hybrid hierarchical composite pyramidal lattice cores. Compos Struct 2013;98:153–9.
[12] Yin S, Wu L, Ma L, Nutt S. Hybrid truss concepts for carbon fiber composite pyramidal lattice structures. Compos B Eng 2012;43:1749–55.
[13] Yin S, Wu L, Ma L, Nutt S. Pyramidal lattice sandwich structures with hollow composite trusses. Compos Struct 2011;93:3104–11.
[14] Lou J, Wu L, Ma L, Xiong J, Wang B. Effects of local damage on vibration characteristics of composite pyramidal truss core sandwich structure. Compos B Eng 2014;62:73–87.
[15] Liu J, Qiao W, Liu J, Xie D, Zhou Z, Wu L, et al. High temperature indentation behaviors of carbon fiber composite pyramidal truss structures. Compos Struct 2015;131:266–72.
[16] Song J, Gao L, Cao K, Zhang H, Xu S, Jiang C, et al. Metal-coated hybrid meso-lattice composites and their mechanical characterizations. Compos Struct 2018;203:750–63.
[17] Yin S, Wang H, Li J, Ritchie RO, Xu J. Light but tough bio-inherited materials: Luffa sponge based nickel-plated composites. J Mech Behav Biomed Mater 2019;94:10–8.
[18] Yin S, Chen H, Li J, Yu TX, Xu J. Effects of architecture level on mechanical properties of hierarchical lattice materials. Int J Mech Sci 2019;157–158:282–92.
[19] Scarpa F, Blain S, Lew T, Perrott D, Ruzzene M, Yates JR. Elastic buckling of hexagonal chiral cell honeycombs. Compos Appl Sci Manuf 2007;38:280–9.
[20] Wang Z. Recent advances in novel metallic honeycomb structure. Compos B Eng 2019;166:731–41.
[21] Hu LL, Luo ZR, Zhang ZY, Lian MK, Huang LS. Mechanical property of re-entrant anti-trichiral honeycombs under large deformation. Compos B Eng 2019;163:107–20.
[22] Fu M, Liu F, Hu L. A novel category of 3D chiral material with negative Poisson's ratio. Compos Sci Technol 2018;160:111–8.
[23] Oftadeh R, Haghpanah B, Papadopoulos J, Hamouda AMS, Nayeb-Hashemi H, Vaziri A. Mechanics of anisotropic hierarchical honeycombs. Int J Mech Sci 2014;81:126–36.
[24] Ajdari A, Jahromi BH, Papadopoulos J, Nayeb-Hashemi H, Vaziri A. Hierarchical honeycombs with tailorable properties. Int J Solids Struct 2012;49:1413–9.
[25] Sun G, Jiang H, Fang J, Li G, Li Q. Crashworthiness of vertex based hierarchical honeycombs in out-of-plane impact. Mater Des 2016;110:705–19.
[26] Chen J, Zhang X, Okabe Y, Saito K, Guo Z, Pan L. The deformation mode and strengthening mechanism of compression in the beetle elytron plate. Mater Des 2017;131:481–6.
[27] Xu J, Wu Y, Wang L, Li J, Yang Y, Tian Y, et al. Compressive properties of hollow lattice truss reinforced honeycombs (Honeytubes) by additive manufacturing: patterning and tube alignment effects. Mater Des 2018;156:446–57.
[28] Yin S, Li J, Liu B, Meng K, Huan Y, Nutt SR, et al. Honeytubes: hollow lattice truss reinforced honeycombs for crushing protection. Compos Struct 2017;160:1147–54.
[29] Kenyon D, Shu Y, Fan X, Reddy S, Dong G, Lew AJ. Parametric design of multi-cell thin-walled structures for improved crashworthiness with stable progressive buckling mode. Thin-Walled Struct 2018;131:76–87.
[30] Ren L, Zhou X, Liu Q, Liang Y, Song Z, Zhang B, et al. 3D magnetic printing of bio-inspired composites with tunable mechanical properties. J Mater Sci 2018;53:14274–86.
[31] Schaedler TA, Jacobsen AJ, Torrents A, Sorensen AE, Lian J, Greer JR, et al. Ultralight metallic microlattices. Science 2011;334(6058):962–5.
[32] Maloney KJ, Roper CS, Jacobsen AJ, Carter WB, Valdevit L, Schaedler TA. Microlattices as architected thin films: analysis of mechanical properties and high strain elastic recovery. Apl Mater 2013;1(2):022106.

[33] Valdevit L, Godfrey SW, Schaedler TA, Jacobsen AJ, Carter WB. Compressive strength of hollow microlattices: experimental characterization, modeling, and optimal design. J Mater Res 2013;28(17):2461–73.
[34] Duan S, Tao Y, Lei H, Wen W, Liang J, Fang D. Enhanced out-of-plane compressive strength and energy absorption of 3D printed square and hexagonal honeycombs with variable-thickness cell edges. Extreme Mech Lett 2018;18:9–18.
[35] George T, Deshpande VS, Wadley HNG. Mechanical response of carbon fiber composite sandwich panels with pyramidal truss cores. Compos Appl Sci Manuf 2013;47:31–40.
[36] Torrents A, Schaedler TA, Jacobsen AJ, Carter WB, Valdevit L. Characterization of nickel-based microlattice materials with structural hierarchy from the nanometer to the millimeter scale. Acta Mater 2012;60:3511–23.
[37] Liontas R, Greer JR. 3D nano-architected metallic glass: size effect suppresses catastrophic failure. Acta Mater 2017;133:393–407.
[38] Cote F, Russell BP, Deshpande VS, Fleck NA. The through-thickness compressive strength of a composite sandwich panel with a hierarchical square honeycomb sandwich core. J Appl Mech T ASME 2009;76.
[39] Chen BC, Zou M, Liu GM, Song JF, Wang HX. Experimental study on energy absorption of bionic tubes inspired by bamboo structures under axial crushing. Int J Impact Eng 2018;115:48–57.
[40] Xu J, Gao X, Zhang C, Yin S. Flax fiber-reinforced composite lattice cores: a low-cost and recyclable approach. Mater Des 2017;133:444–54.
[41] Zhang Y, Liu Q, He Z, Zong Z, Fang J. Dynamic impact response of aluminum honeycombs filled with Expanded Polypropylene foam. Compos B Eng 2019;156:17–27.
[42] Fu N, Liu Y, Liu Y, Lu W, Zhou L, Peng F, et al. Facile preparation of hierarchical TiO2 nanowire–nanoparticle/nanotube architecture for highly efficient dye-sensitized solar cells. J Mater Chem A 2015;3:20366–74.
[43] Zhang X, Zhang H. Numerical and theoretical studies on energy absorption of three-panel angle elements. Int J Impact Eng 2012;46:23–40.
[44] Chen T, Zhang Y, Lin J, Lu Y. Theoretical analysis and crashworthiness optimization of hybrid multi-cell structures. Thin-Walled Struct 2019;142:116–31.
[45] Qiu N, Gao Y, Fang J, Feng Z, Sun G, Li Q. Theoretical prediction and optimization of multi-cell hexagonal tubes under axial crashing. Thin-Walled Struct 2016;102:111–21.
[46] Zhang X, Zhang H. Energy absorption of multi-cell stub columns under axial compression. Thin-Walled Struct 2013;68:156–63.
[47] Avalle M, Belingardi G, Montanini R. Characterization of polymeric structural foams under compressive impact loading by means of energy-absorption diagram. Int J Impact Eng 2001;25(5):455–72.
[48] Duarte I, Vesenjak M, Krstulović-Opara L. Compressive behaviour of unconstrained and constrained integral-skin closed-cell aluminium foam. Compos Struct 2016;154:231–8.
[49] Queheillalt DT, Wadley HNG. Cellular metal lattices with hollow trusses. Acta Mater 2005;53(2):303–13.
[50] Harris JA, Winter RE, McShane GJ. Impact response of additively manufactured metallic hybrid lattice materials. Int J Impact Eng 2017;104:177–91.